



Parametric optimization of friction stir welding of AA 6101 T-64 and pure Cu using response surface methodology

S. K. Nirgude¹ · S. D. Kalpande²

Received: 10 November 2022 / Accepted: 17 January 2023 / Published online: 7 February 2023
© The Author(s), under exclusive licence to Springer-Verlag France SAS, part of Springer Nature 2023

Abstract

The friction stir welding (FSW) process was used to join electrical grade aluminium alloy 6101 T-64 and pure Cu plates and optimized using the Box–Behkan approach of response surface methodology. The tool rotational speed, traverse speed, tool offset, and tool tilt angle were deemed to be relevant parameters since they have a considerable significance on the weld joint properties. By using mathematical models, the relationship between welding parameters and responses (tensile strength σ_s and electrical resistivity ρ) is examined. The responses are maximized or minimized in these models. Response plots produced from mathematical models are used to analyze the interaction effects of the FSW parameters on the output responses. Through the use of the analysis of variance (ANOVA) method, the constructed models are validated. The results of the experimental research demonstrated that a wide range of FSW settings can be used to construct sound weld joints without defects. The findings from the tensile strength ANOVA table showed that the tool rotational speed and tool offset were significant parameters, however the traverse speed and tool tilt angle were not significant parameters for tensile strength. From ANOVA table of electrical resistivity all parameters were found significant for electrical resistivity. The experimental results and predicted models showed good agreement. The microhardness study at optimized welding parameters revealed the variations in microhardness distribution in different regions. It is found that the microhardness distribution was higher in the bottom region followed by top region and middle region.

Keywords Friction stir welding (FSW) · Box–Behkan design method · Response surface methodology (RSM) · Tensile strength · Electrical resistivity · Microhardness

1 Introduction

The Welding Institute (TWI) invented the friction stir welding (FSW) process in 1991 as a “green technology” [1, 2, 6, 8, 10]. It’s a solid state joining technique carried at the recrystallization temperature. A rotating tool pin with an unique feature is inserted between the base materials’ adjacent edges. Frictional heating between the material surface and the tool shoulder leads the material to soften. A solid state weld joint is formed when the softened material is stirred by the tool pin [24, 27, 31, 32]. The process

reduces defects like solidification cracking and intermetallic compounds (IMCs) formation since it works below the material’s melting point [24]. FSW joints shows low distortion and greater weld strength [23, 27]. The process is used to join materials that are similar and dissimilar. In the nuclear, aerospace, electrical, and electronics industries, joints made of different materials are used for weight & cost reduction and improvement in productivity [1, 5, 6, 9, 13, 14]. Copper and aluminum has good corrosion resistance, mechanical properties, heat and electrical conductivities [17, 27]. The common industrial applications of Al–Cu joint are in bus-bars, electrical connectors, bimetals, heat exchanger tubes, heat sink, and refrigeration tubes [1, 5, 6, 9, 14]. Cost, mass and weight reduction is required in present days engineering applications [20]. Both materials are having different physical, chemical, flow stress, and mechanical properties. The IMCs affects the mechanical and electrical properties [7, 9, 30]. Incorrect parameter selection results in poor stirring, and

✉ S. K. Nirgude
snirgude299@gmail.com; shyamkalpande@gmail.com

¹ Mechanical Engineering Department, MET’s IOE Bhujbal Knowledge City, Nashik, India

² Mechanical Engineering Department, Guru Gobind Singh COE & RC, Nashik, India

insufficient heat input causes defects including tunnel, cavities, and voids to occur in the FSW of Al–Cu. So optimization of the FSW of Al–Cu is essential for sufficient material flow around the tool pin, prevention of the brittle IMCs formation, for commercialisation and sound joint formation during FSW. [7, 9, 11, 13, 18, 20]. The optimization model can be used to determine the best input process parameter settings to achieve the desired performance of the weld joint and examine the effects of different input process parameters on the responses. Esmaili et al. [2] reported that during the FSW of aluminium and brass, a slight tool pin offset towards the softer material leads a cavity defect to form behind the tool pin. Genevois et al. [3] claimed that the tensile strength in the Al–Cu FSW joint is improved by the formation of a thin IMC layer in the stir zone (SZ) created by interdiffusion bonding. Felix et al. [4] found that dispersion strengthening of the tiny particles in SZ results in higher weld joint tensile strength. Wei et al. [5] revealed that the copper side of the SZ had a higher distribution of hardness than the aluminium side, and that the hardness distribution at the bottom of the SZ was higher than that in the top and middle region. Liu et al. [6] pointed out that the Al–Cu FSW joint's tensile strength is constrained by the presence of IMCs. Galvao et al. [7] concluded that at lower tool rotational speed a thin IMC layer formed whereas at higher tool rotational speed a thick IMC rich structure was observed. Fotouchi et al. [8] observed that the tool offset reduces the void defect formation. Also improper mixing of the material and formation of IMCs are the reasons of reduced tensile strength of the weld joint. Galvao et al. [11] observed that the rate of IMC formation is reduced by the tool's offset towards the softer material aluminium side. Beygi et al. [12] revealed that the bands in the Cu structure are a result of the material flow in the SZ. The hardness values are increased by the presence of Al particles with Al–Cu IMC in the fine grain structure. Xue et al. [13] revealed that the formation of thin and continuous layer Al–Cu IMC provides good metallurgical bonding. Whereas the more Cu particles and IMC layers generated at the lower part of SZ forms composite structure with elevated hardness level. Saeid et al. [14] revealed that a dark region with IMCs Al_4Cu_9 and Al_2Cu was seen close to the Al–Cu region during analysis of the Al–Cu FSW lap joint. With the traverse speed increased, the occurrence of microcracks was also decreased. At a faster traversal speed, the cavity was formed. Shojaeefard et al. [15] observed in ANOVA that the most important factor influencing the formation of sound FSW joints is the tool rotational speed. Bisadi et al. [16] observed higher hardness level in the SZ of the weld joint due to the small grain size. Zhang et al. [17] reported that the formation of dislocation loops and a high dislocation density are induced by the SZ's increased hardness. Won-Bae et al. [18] pointed out that a thick IMC layer significantly

reduces the weld joint's tensile strength and electrical resistance. Kah et al. [19] claimed that traverse speed, heat input during process, and the thermal properties of the base materials had a significant impact on the IMC formation and its influence on welding properties. Kerrar et al. [21] revealed that maximum hardness was seen as in the SZ as compared to that of other two zones. Rai et al. [22] stated that the weld joint quality is depending on the tool material and designs. W based materials were found affordable for use. Dharmalingam et al. [23] pointed out that H 13 tool material has been employed by numerous studies. A rise in tool rotational speed also resulted in an improvement in surface integrity. Zhang et al. [25] observed that the taper profile pin exhibits more frictional heat and more plastic deformation which forms sound weld joint. Zhao et al. [26] suggested the preheating process before FSW of Al–Cu. It helps to grain refinement and strong weld joint formation. Akinlabi et al. [27] observed that the grains were recrystallized at the interfacial zone with decrease in grain size. Also higher hardness was seen in that region because of strain hardening and presence of IMCs. With increased heat input and speed, the weld joint's electrical resistivity increased. At the optimum process parameters settings of tool rotational speed of 950 rpm and traverse speed of 50 mm/min with 18 mm tool shoulder diameter, higher tensile strength and decreased electrical resistivity of the Al–Cu joint was observed. Beygi et al. [28] pointed out that the contact surfaces between the tool shoulder and the plate surface influences the material flow and microstructure of the weld joint. Bhattacharya et al. [29] reported that the temperature cycle has a significant impact on the tensile strength of the weld joint. Wei et al. [32] revealed that the highest tensile strength obtained at 950 rpm and 0° angle of inclination. The joint defects and IMC formation affects the interfacial resistance. Bakhtiari et al. [33] observed that the hardness value in the SZ depend on the grain size and IMC. Raj et al. [34] revealed that thin layer of IMC at the interference improves the strength of the weld joint, but a thick IMC layer weakens the weld joint. Koilraj et al. [35] using the Taguchi approach, the FSW process parameters were optimised. The tool shoulder to pin diameter ratio, pin diameter, and traverse speed were all significant factors in the formation of sound joints, according to an ANOVA table. Sharma et al. [36] observed according to Taguchi and TOPSIS techniques of optimization, tool rotational speed was the most significant parameter, followed by traverse speed and tool pin offset. Varma et al. [37] revealed that the values of tensile strength and % elongation increase and decrease as FSW parameters such as tool rotational speed, tool tilt angle, and traverse speed are increased. Elnabi et al. [38] pointed that high heat input leads to flash defect formation in the weld joint. Shanavas et al. [39] applied the RSM optimization technique and reported that the tool tilt angle has a significant role in FSW, followed by the tool rotational speed. Jabbari et al.

[46] revealed that the grain size increases in the SZ of the weld joint as tool rotational speed increases. In the SZ, the average grain size decreased but the tensile strength was increased. Sundaram et al. [47] used CCD design matrix of RSM method of optimization for FSW of Al/Mg dissimilar materials and revealed that the tool plunge rate influences the tensile shear fracture load. Sabry et al. [48] optimized the underwater FSW process of Al plates using fuzzy logic technique and found the adequate prediction of the output process parameters. Van et al. [49] used the genetic algorithm (GA) and Taguchi-based neuro-based fuzzy inference system (ANFIS) to optimise and analyse the significance of FSW process parameters during FSW of AA 6061 plates. Prabhu et al. [50] optimized the FSW of AA6061/TiO₂ composites by using teaching learning based optimization (TLBO) algorithm. Hussien et al. [51] utilized the particle swarm optimization (PSO) to optimise the FSW process for aluminium plates. The findings of the comparison revealed that the modified PSO approach was more accurate than the conventional PSO approach.

As it was previously mentioned, a variety of optimization strategies for FSW of Al–Cu have been covered in the literature, including introduction, applications, significance, grades of material, material thickness, significant parameters, parameter combinations, and introduction. However, there is a lack of research on the optimization of FSW parameters for electrical grade AA 6101 T-64 and pure Cu. The novelty of this research work is that it optimises the process variables for electrical resistivity and tensile strength. Additionally, it discusses the microstructure of the weld joint and the distribution of microhardness, as well as the impact of process parameters on output responses.

2 Methodology

The extensive literature review was taken into consideration when selecting the important process parameters. The number of trials has been conducted for selection of the range of input parameters. Four significant parameters and three levels were selected for research study namely tool rotational speed, traverse speed, tool offset, and tool tilt angle with lower, middle and upper level as these parameters significantly affect the weld joint performance. According to the applicability of the selected weld joint the tensile strength and electrical resistivity are the most important output parameters. A Box–Behkan response surface method design matrix with 27 runs was used for experimentation. The parameters' upper and lower limit was coded as 1 and -1, respectively. The parameters at the middle level were coded as 0. On the basis of this range FSW process parameters were selected. Electrical grade aluminum alloy 6101-T64 and pure copper bus bar of 4 mm thickness is widely used in electrical applications [55]. So the 4 mm thick plates of both materials were selected

for research study. The length of weld run was selected by considering the previous extensive literature. The width of the each plate was selected by considering the clamping area required to gooseneck clamp for clamping in the welding fixture and free space required for the traversing of the tool during welding. The dimensions of the welding plates were 150 mm × 75 mm × 4 mm. Table 1 and Table 2 provide the chemical properties of the base materials. The oxide film from the surfaces of plates was removed by grinding with grit paper. The plates were placed on backing plate to avoid sticking the plates with the fixture surface after welding. The plates were clamped rigidly in the fixture by the gooseneck clamps to avoid relative movement of the plates during welding. A cylindrical tool with a taper (taper angle: 10° 49' 15'') made of H 13 tool steel specifications as: shoulder diameter 20 mm, pin length 3.7 mm, smaller pin diameter 5 mm, and larger pin diameter 6 mm [23, 25]. The tool was offset towards softer material Al side. For sound joint formation, Al was placed on the retreating side and Cu on the advancing side in the welding fixture [40]. Tool plunge depth and dwell time were 0.1 mm and 20 s respectively. Figure 1 and Fig. 2 illustrate the schematic diagrams for the welding setup with strategy and the FSW tool, respectively.

After the FSW process the standard metallographic steps were followed for sample preparation. For macroscopic and microscopic examination, the samples were cut on a WEDM machine perpendicular to the welding direction. The polishing of the observation surface of the samples was done with 80, 220, 320, 400, 600, and 1000 grit size abrasive papers on microgrinder. The diamond paste and microfinishing cloth were used for microfinishing of the samples. The prepared samples were then chemically etched at room temperature using two different agents. Keller's reagent etched the Al side (190 ml H₂O, 3 ml HCL, 5 ml HNO₃ and 2 ml HF). 25 ml H₂O, 25 ml NH₄OH, and 10 ml H₂O₂ were used to etch the Cu side. Using a (OLYMPUS) microscope camera, the weld joint macrographs of the weld direction cross-sections were observed. An optical microscope was used to investigate the Al–Cu interface and the SZ microstructure (OLYMPUS GX 51). Using a Vickers microhardness tester on the welding direction cross-section of the welded joint samples, the microhardness distribution in various weld joint regions was measured. For measurement, a load of 200 g with a dwell period of 10 s was used. Three specimens were cut for each set of parameters from the welded plates across to the welding direction before tensile testing. Using a tensile testing machine with a constant displacement rate of 1 mm/min at room temperature, the tensile tests were carried out. The dimensions of the specimens were in accordance with ASTM-E8. Figure 3 and Fig. 4, respectively, shows a 3D diagram of a tensile test specimen and a 2D diagram of a specimen prepared for tensile testing.

Table 1 Chemical properties of AA 6101- T64 [36]

Si	Fe	Zn	Mg	Sn	Ti	V	Pb	Cr	Sr	Al
0.374	0.167	0.025	0.482	0.003	0.002	0.008	0.019	0.06	0.004	98.879

Table 2 Chemical properties of pure cu [46]

Zn	Sn	Pb	P	Si	Fe	Cu	Balance
0.023	0.008	0.004	0.013	0.008	0.008	99.935	Al

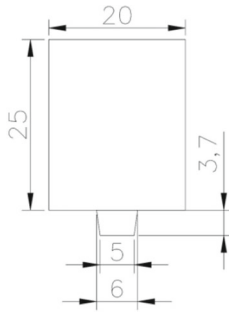


Fig. 1 FSW tool schematic [25]



Fig. 2 FSW set up with welding strategy

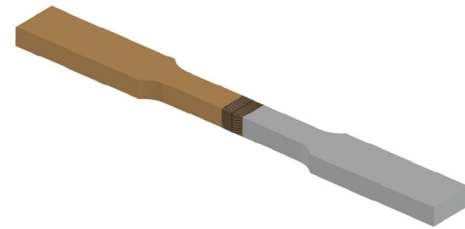


Fig. 3 3D diagram of tensile strength test specimen

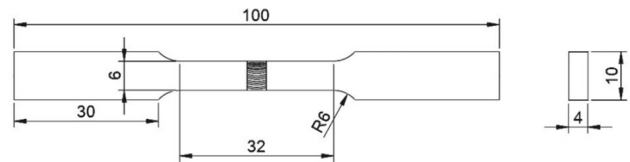


Fig. 4 2D tensile strength test specimen preparation as per ASTM E8 standard

3 Development of mathematical model

The input parameters and the responses were mathematically correlated using the response surface methodology. Data from 27 experimental runs is used as input. The functions of tool rotational speed (N), traverse speed (S), tool offset (O), and tool tilt angle (A) are assumed to predict the responses tensile strength and electrical resistivity. These are expressed as:

$$\text{Tensile strength} = f(N, S, O, A) \tag{1}$$

$$\text{Electrical resistivity} = f(N, S, O, A) \tag{2}$$

The response surface is represented by The second order polynomial regression equation is given as, [53]:

$$Y = b_0 + \sum b_i x_i + \sum b_{ii} x_i^2 + \sum b_{ij} x_i x_j \tag{3}$$

The above equation may be written as,

$$Y = b_0 + b_1 N + b_2 S + b_3 O + b_4 A + b_{11} N^2 + b_{22} S^2 + b_{33} O^2 + b_{44} A^2 + b_{12} N x S + b_{13} N x O + b_{14} N x A + b_{23} S x O + b_{24} S x A + b_{34} O x A \tag{4}$$

where the coefficients $b_1, b_2, b_3,$ and b_4 represent the linear, quadratic, and interaction coefficients, respectively, and b_0 is the mean value of the response variables. A quadratic term is a coefficient with the values $b_{11}, b_{22}, b_{33},$ and b_{44} . Interaction terms are represented by the coefficients $b_{12}, b_{13}, b_{14}, b_{23},$ and b_{34} . At a 95% confidence level, the coefficients were evaluated and tested. A mathematical model was developed to predict the tensile strength and electrical resistivity of the weld joints.

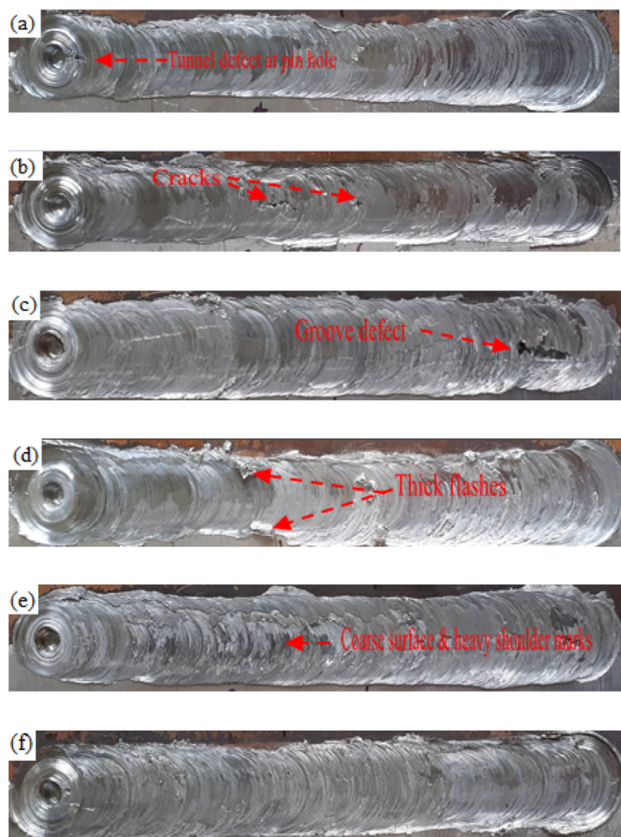


Fig. 5 Joint surface appearance of defective joints **a–e**. Surface appearance of the weld joint prepared at optimized FSW process parameters **(f)**

$$\begin{aligned} \sigma_s = & -215.4 + 0.7680N + 0.679S + 22.5O + 9.98A \\ & - 0.000419N^2 - 0.00683S^2 - 13.97O^2 - 2.216A^2 \\ & + 0.000074NxS + 0.0085NxO - 0.00143Nx A \\ & - 0.048SxO - 0.0227SxA + 1.33OxA \end{aligned} \quad (5)$$

$$\begin{aligned} \rho = & 0.0264 - 0.000020N + 0.000403 S + 0.00341O \\ & - 0.00426A + 0.000000N^2 - 0.000001S^2 \\ & - 0.00255O^2 + 0.000401A^2 - 0.000000NxS \\ & - 0.000004NxO + 0.000001N x A - 0.000015SxO \\ & - 0.000011SxA + 0.00106OxA \end{aligned} \quad (6)$$

4 Joint surface appearance defective and optimized weld joint

Figure 5 represents the Al–Cu weld surface appearance of the weld joints with defects and the joint with optimised process parameters. The joint defect formation and poor weld structure are caused by the insufficient material flow during FSW. One of the key factors in defect generation is

the selection of improper process parameters [2]. The tunnel and crack defects were present at higher tool traverse speeds of 70 mm/min and lower tool rotational speeds of 700 rpm, as shown in Fig. 5(a, b), respectively. The crack defect was formed due to insufficient heating and less softening for material flow [2]. The groove defect was also seen due to insufficient heating is shown in Fig. 5c. Figure 5f illustrates how the optimum parameters of the tool's rotational speed (930 rpm), traverse speed (47 mm/min), tool offset (1.1 mm), and tool tilt angle (2°) produced a very nice joint surface appearance. Tool pins rotate at 1100 rpm, which is a higher tool rotational speed, under especially hot processing conditions [45]. Near the tool shoulder, the softened material expelled out [21]. Figure 5d shows the flash defect that results from higher rotation speed.

4.1 Weld joint interface microstructure

In Fig. 6a–o, an optical micrograph of the microstructures of the weld joints is shown at various combinations of welding parameters and weld areas (retreating side, weld zone, and advancing side). The optical macrograph of the cross section of the welded specimen perpendicular to the welding direction taken at optimal process parameters is shown in Fig. 7. There was no micro cracks or voids observed in the weld joint after macroscopic examination.

The material exhibited a complex mixing behaviour along the interfaces after being stirred, according to microscopic investigations. The injected Cu particles in the SZ create a strong Al–Cu joint on the retreating side (Fig. 6a, d, g, j, and m). It was possible to see the sharp interface, which resembled material flow, in the weld joint's side [24]. Due to heat input from the tool during stirring, equiaxed grain structure of the Al matrix was found in the TMAZ- SZ region [54]. In contrast to the deformed grain structure observed in the TMAZ-SZ zone, larger and longer grains were seen in the HAZ. The width of the grains was also growing in the TMAZ-SZ region as the tool rotation speed increased. The recrystallization in this area is enhanced by the tool pin's offset towards the side of soft material. Al–Cu material was mixed in the SZ to form a layered structure (Fig. 6b, e, h, k, and n). Due to variations in the heat input, the homogenous and inhomogeneous microstructure was seen at various tool rotational speeds and traverse speeds [43]. In the SZ, a typical vortex-like microstructure was seen (Fig. 6h, k, and n) as well as a whirl-like microstructure (Fig. 6e). At the Cu- Al interface on the advancing side, TMAZ and SZ were seen. The tool rotational speed and traverse speed, which have a significant impact on heat input during welding, were found to change the width of the SZ. Additionally, the TMAZ on the advancing side was seen to be less than that on the retreating side. The material characteristics are changed by recrystallization in the TMAZ-SZ zones on both sides [16].

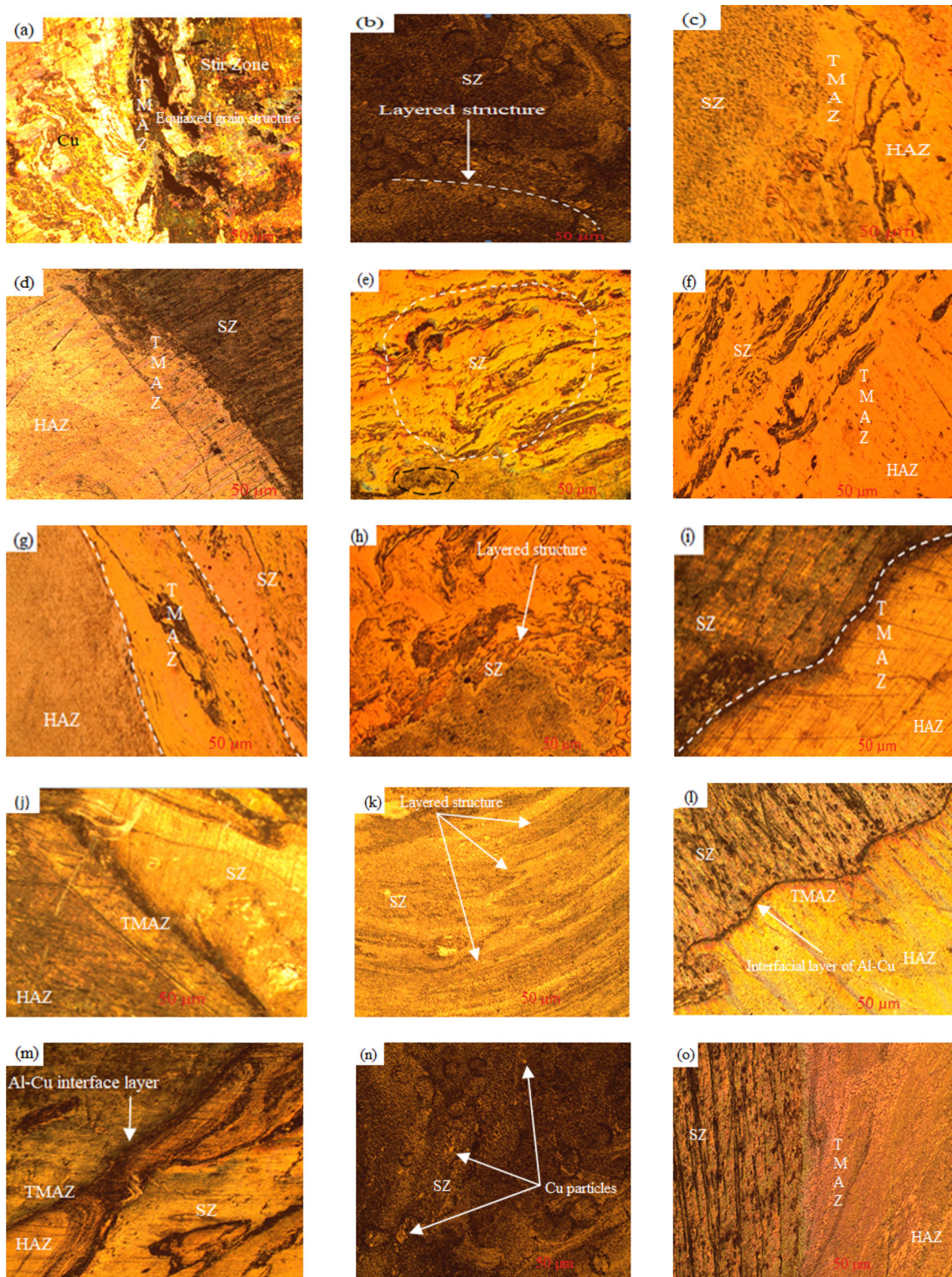


Fig. 6 Optical micrographs of microstructures presenting different weld regions at various combinations of set of parameters during validation

test. **a–c** validation test for set 1, **d–f** validation test for set 2, **g–i** validation test for set 3, **j–l** validation test for set 4, and **m–o** validation test for set 5

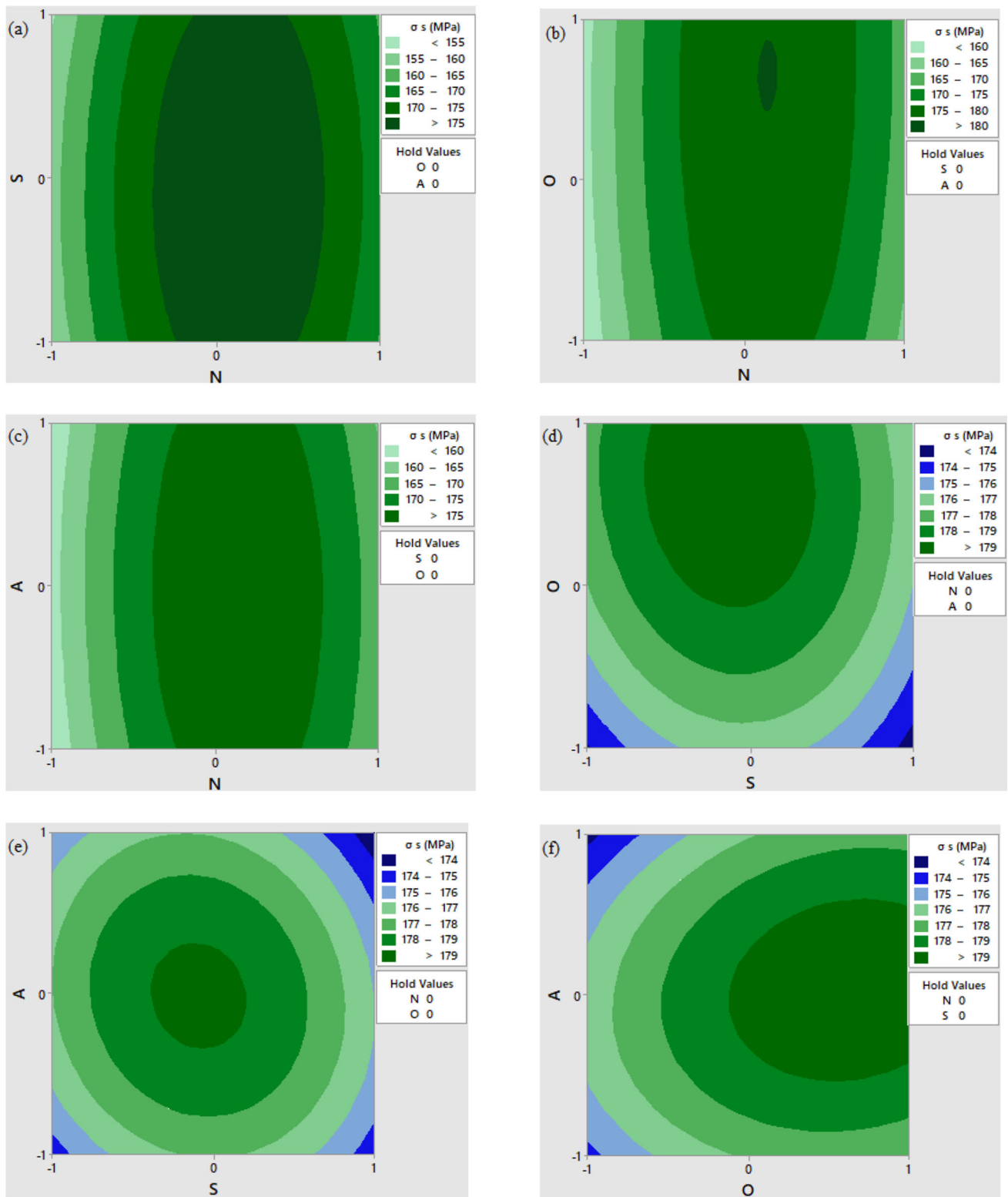


Fig. 7 Contour plots of FSW parameters and σ_s

Table 3 The levels of the FSW process parameters for experimentation

Sr. no.	Input parameters	Notation	Unit	Levels		
				− 1	0	1
1	Tool Rotational speed	N	rpm	700	900	1100
2	Traverse speed	S	mm/min	30	50	70
3	Tool offset	O	mm	0.6	0.9	1.2
4	Tool tilt angle	A	Degrees	1	2	3

Table 4 The Box–Behkan design matrix experiment's results

Trial run	Parameters				σ_s (MPa)	ρ ($\mu\Omega\text{m}$)
	N	S	O	A		
1	0	0	0	0	179.15	0.030
2	0	1	1	1	171.57	0.027
3	0	0	− 1	1	172.61	0.030
4	0	0	0	0	177.55	0.030
5	− 1	0	0	− 1	155.17	0.029
6	1	0	− 1	0	163.92	0.037
7	0	− 1	0	− 1	176.45	0.032
8	0	0	0	0	179.73	0.030
9	1	1	0	0	163.54	0.032
10	− 1	0	0	1	157.36	0.026
11	0	− 1	0	1	175.87	0.030
12	1	0	0	1	164.21	0.035
13	0	− 1	1	0	174.94	0.030
14	0	− 1	− 1	0	174.76	0.031
15	1	− 1	0	0	163.92	0.039
16	− 1	0	− 1	0	153.58	0.028
17	0	0	− 1	− 1	175.19	0.032
18	0	1	− 1	0	174.92	0.029
19	0	0	1	0	179.91	0.029
20	0	0	1	− 1	176.55	0.030
21	− 1	1	0	0	154.04	0.026
22	1	0	1	0	171.34	0.033
23	1	0	0	− 1	163.16	0.037
24	0	1	0	− 1	174.63	0.030
25	0	1	0	1	174.27	0.026
26	− 1	0	1	0	158.96	0.025
27	− 1	− 1	0	0	155.61	0.027

5 Evolution of results

5.1 Location of the fracture during tensile strength testing

The weld joints made with a tool rotational speed of 700 rpm, moving at a traverse speed of 30 mm/min, and tilting at an angle of 1° fractured in the SZ during tensile testing. By

further changing the welding parameters, the fracture location was shifted from the thermomechanically affected zone (TMAZ) to the SZ and back again. This indicates that the welding parameters have no effect on the fracture site Table 3.

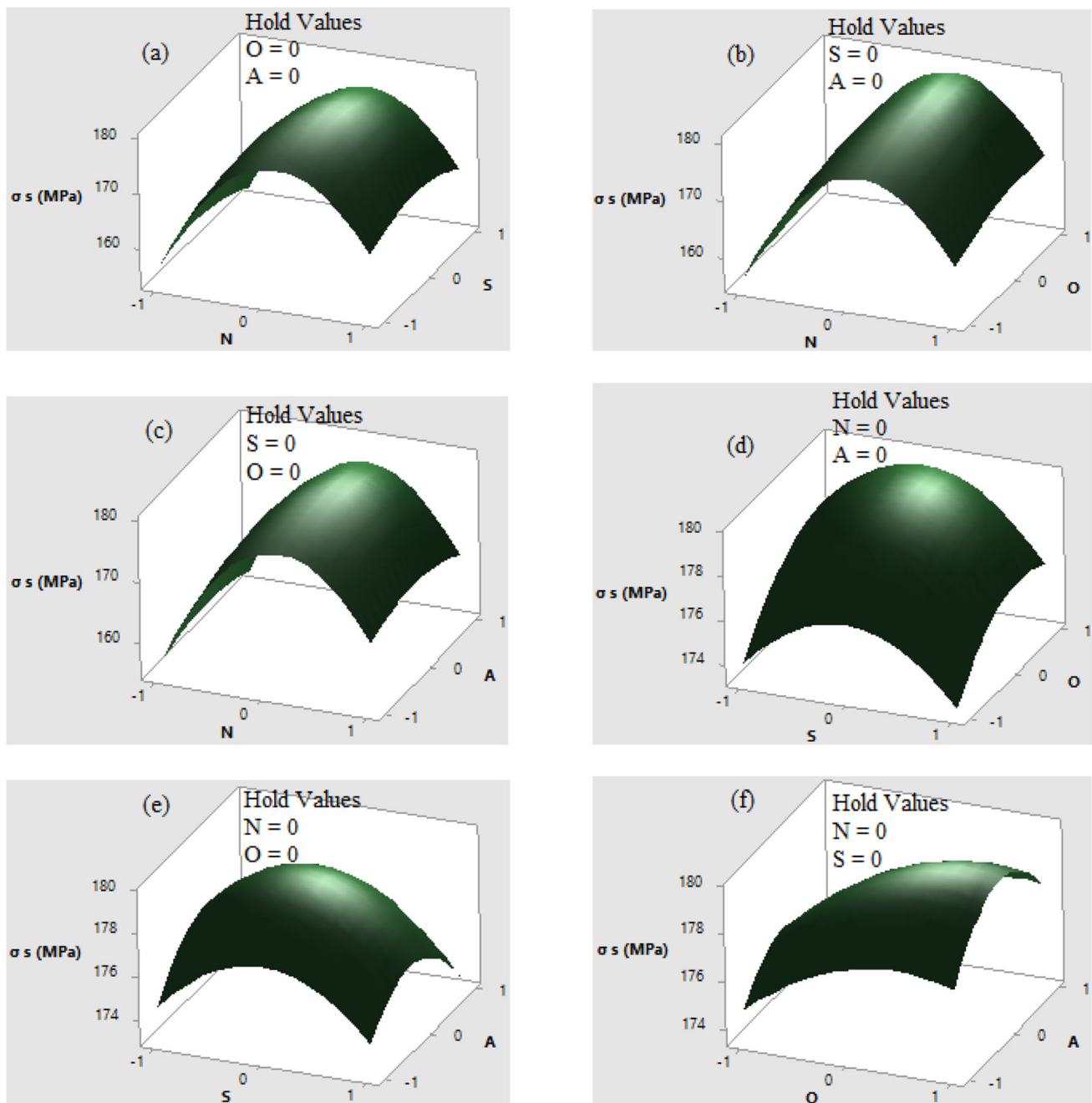


Fig. 8 FSW parameter and σ_s response surface plots

5.2 Effects of parameters on tensile strength

Tensile strength tests were performed to analyse the impact of FSW factors on the Al–Cu weld joint quality. As can be seen in Fig. 3 and Fig. 4, the specimens were prepared in accordance with ASTM E8 standards. Table 4 displays the experimental results of the tensile test. Figure 8 and Fig. 9 shows the interface effects of FSW process parameters on the joint's tensile strength. Figure 10 shows direct effect plots of the FSW parameters on the responses. Figure 11 and Fig. 12

show the interaction effects of FSW parameters on tensile strength. With increases in tool rotational speed, traverse speed, tool offset, and tool tilt angle, the tensile strength increased and then decreased after reaching its maximum value. Table 5. Statistical results show good agreement with the results of R^2 value.

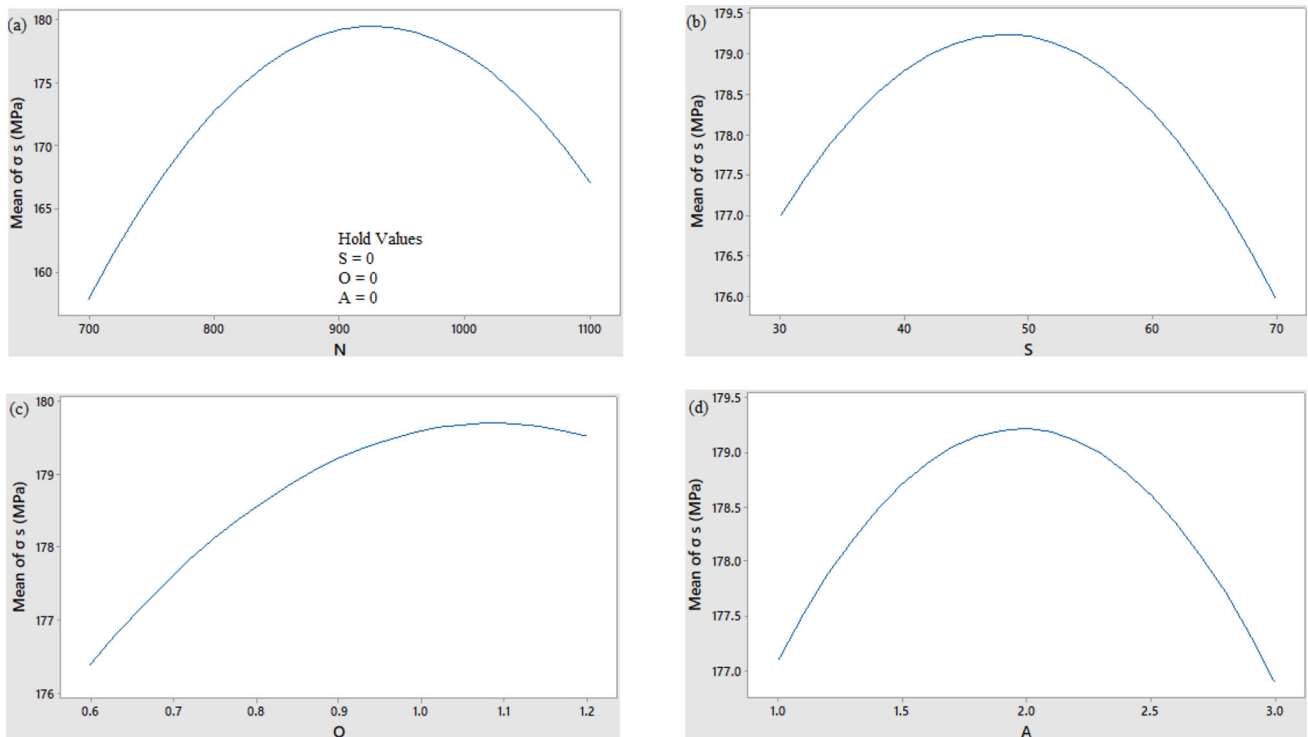


Fig. 9 Direct effects of FSW parameters on σ_s include **a** tool rotational speed, **b** traverse speed, **c** tool offset, and **d** tool tilt angle

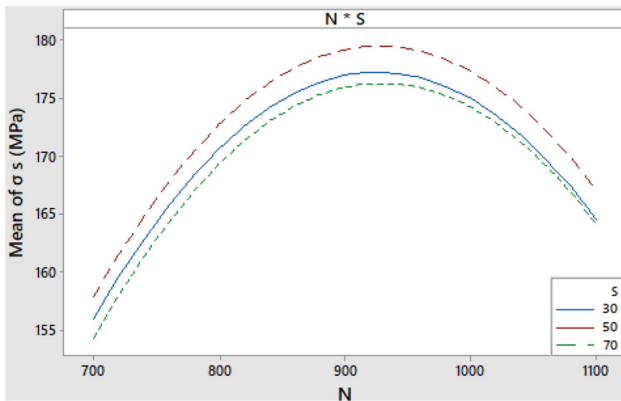


Fig. 10 Effects of N and S interacting on σ_s

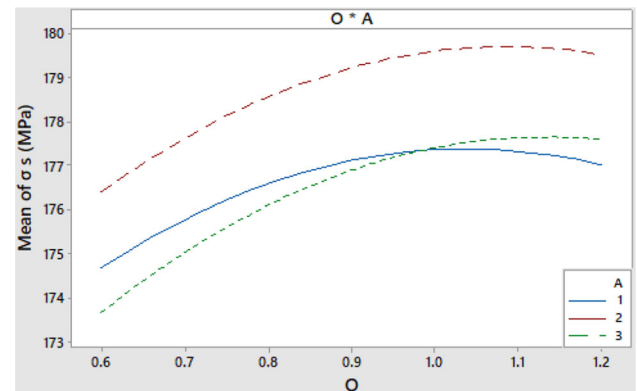


Fig. 11 Effects of O and A interacting on σ_s

5.2.1 Effect of tool rotational speed

The effect of tool rotational speed on tensile strength of the weld joint is shown in Fig. 9a. Lower tensile strength was observed relative to higher tensile strength at a lower tool rotational speed of 700 rpm. It was as a result of the Cu elements in the Al matrix not being sufficiently heated and mixed. With an increase in rotational speed, the joint's tensile strength gradually grew. At 900 rpm, the maximum tensile strength of 179.91 MPa was achieved because at this speed, the Cu and Al matrix combine satisfactorily [7]. Additionally, it was found that the tensile strength decreased from 900 to

1100 rpm as the tool's rotational speed increased. More heat was generated as a result of the base material plate and tool shoulder face coming into contact for a longer period of time. This significantly promotes IMC thickening in the SZ [40]. At high tool rotational speeds, the tensile strength was decreased as the IMCs in the weld nugget zone increased [7].

5.2.2 Effect of traverse speed

Lower tensile strength was observed due to excessive heating and flow stress difference between Al and Cu in the nugget zone at lower traversal speeds of 30 mm/min because the



Fig. 12 Macrograph showing the cross section of the FSW sample for the confirmation test for the tensile strength experiment

Table 5 Statistical results for tensile strength

Response	R ²	Adjusted R ²	Standard error %
Tensile strength	0.975	0.946	2.04427

turbulent material flow results in lower strength. The micro crack begins to develop at high heat input and leads the weld joint to fail. As seen in Fig. 9b, thick brittle intermetallic compounds also developed, decreasing the tensile strength. The required heat input increases the tensile strength as the traverse speed is increased to 50 mm/min. The size of the recrystallized fine grains decreased at this stage. It grows the grain boundary. At a traverse of 50 mm/min, the turbulent flow is also normalised. The heat input decreases as traverse speed is increased to 70 mm/min. The rate of plasticization is slowed, and improper material mixing is prevented. Therefore, at lower tensile strengths, the weld joints failed.

5.2.3 Effect of tool offset

The effect of tool offset toward the side of aluminium on the joint's tensile strength is shown in Fig. 9c. Lower tensile strength was indicated by the tool pin's 0.6 mm offset in favour of the Al side. It results in void defects and poor bonding. In SZ, more Cu atoms produced brittle IMC, lowering the tensile strength [42]. Improvement in tensile strength was observed as tool offset was extended to 0.9 and 1.2 mm. Less Cu was present in the SZ, and less Cu interacts with Al to produce fewer IMCs. As the tool offset was increased, the joint's tensile strength increased [7, 9, 10, 42].

5.2.4 Effect of tool tilt angle

The impact of tool tilt angle on joint tensile strength is presented in Fig. 9d. It was observed that the tensile strength increased as the tool tilt angle increased, then decreased as the angle increased. The heat generation is high at a 1° tool tilt angle. The high heat generation was decreased by raising the tool tilt angle by 2°, which improved the tensile strength of the weld joint. The experiment's observations showed that as the tool tilt angle increased, the tensile strength initially increased before decreasing as the tool tilt angle approaches to 3° [46, 47].

5.3 Electrical resistivity

SIGMASCOPE electrical resistivity measurement equipment was used to determine the weld joint's electrical resistivity. The weld joint electrical resistivity was observed in the range of 0.025–0.039 $\mu\Omega\text{m}$. The variation in the resistivity was observed because of differences in heat input, material mixing and microstructure variation during FSW. Figure 13 and Fig. 14 show contour plots and surface plots illustrating the influence of process factors on electrical resistivity. Figure 15 shows direct effect plots showing the influence of FSW parameters on electrical resistivity. The interface effects of FSW process parameters on the electrical resistivity of the weld joint are shown in Fig. 16 and Fig. 17. With an increase in tool rotational speed, the electrical resistance increased. However, as traverse was increased, it was found that electrical resistivity decreased along with tool offset and tool tilt angle.

5.3.1 Effect of tool rotational speed

The effect of tool rotational speed on electrical resistivity of the weld joint can be seen in Fig. 15a. Higher electrical resistance was observed at higher tool rotational speeds of 1100 rpm. IMCs thicken at this temperature as a result of the increased heat input. IMCs resulted in an increase in electrical resistance. As there was no heat input and the thickness of the IMCs in the weld region was not significantly increased, the lowest electrical resistance was observed at the lowest tool rotational speed of 700 rpm. [41].

5.3.2 Effect of traverse speed

Figure 15b shows how traverse speed influences the joint's electrical resistivity. Like rotational speed, traverse speed was found to be significant because it influences how much heat is

Introduced during welding. The lowest traverse speed of 30 mm/min resulted in a higher electrical resistance of 0.039 $\mu\Omega\text{m}$. At this temperature, IMCs thickened significantly [12, 41]. In contrast, electrical resistivity during FSW at higher traverse speeds up to 70 mm/min decreases by 0.025 $\mu\Omega\text{m}$ as heat input decreases and IMC size also decreases.

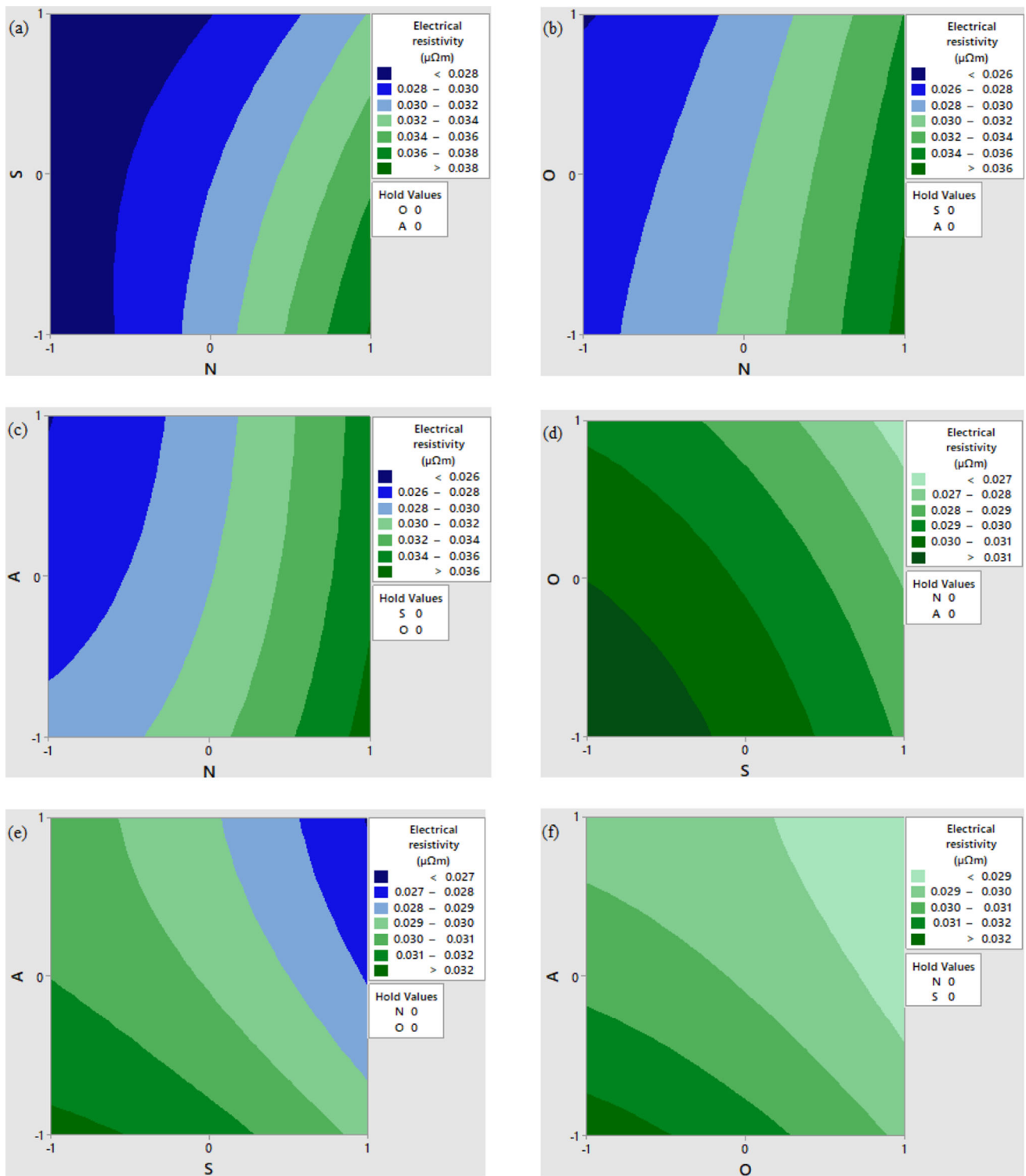


Fig. 13 Contour plots of FSW parameters and ρ

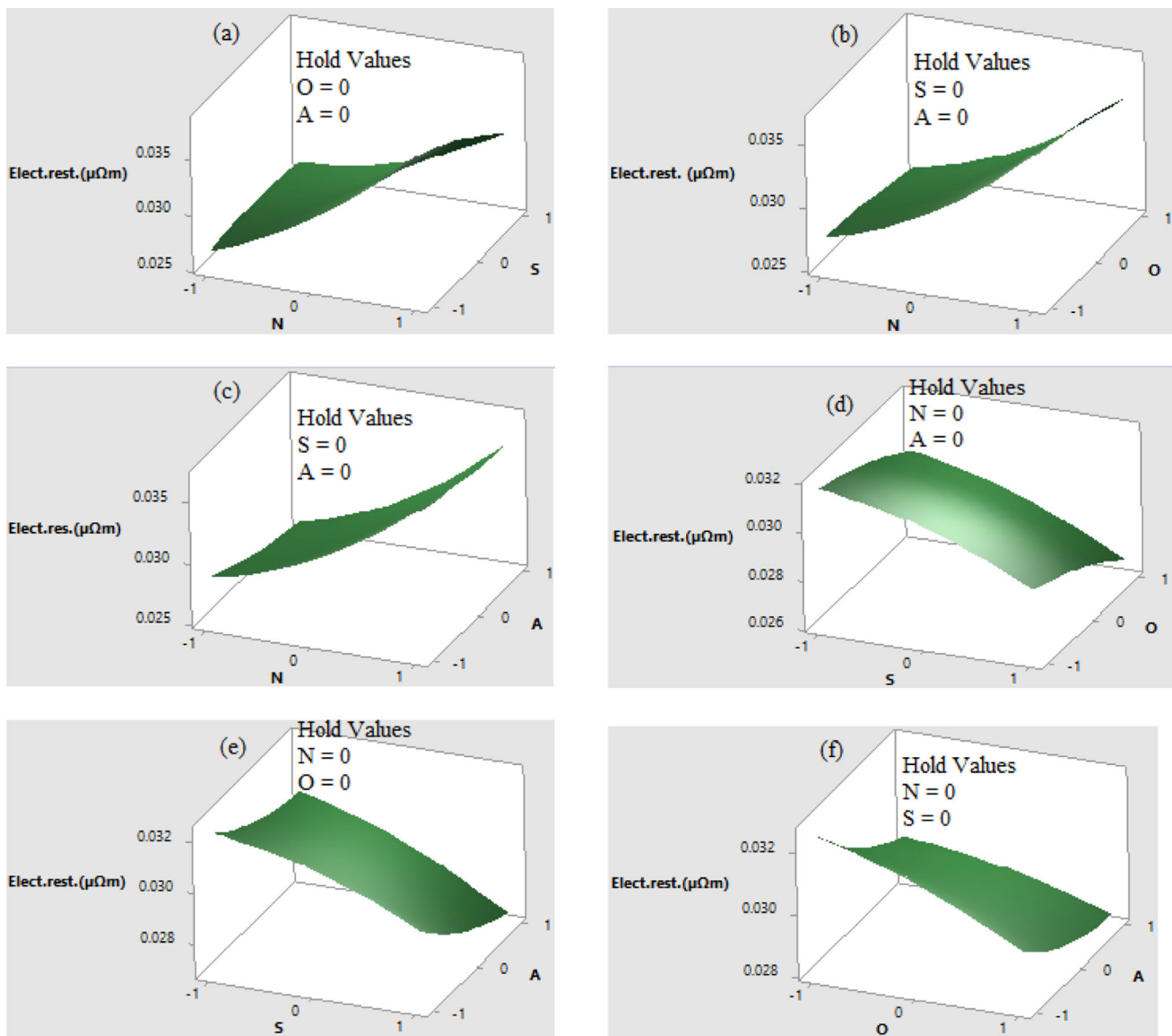


Fig.14 Response surface plots of the FSW parameters and ρ

5.3.3 Effect of tool offset

More Cu particles interact with the Al matrix at the lower tool pin offset toward the Al side, producing thick, hard IMCs. The influence of tool offset on the joint's electrical resistivity is seen in Fig. 15c. Higher resistivity has been the outcome. The small amount of Cu particles mix with the Al matrix as the tool pin offset toward the Al side increases, which promotes the formation of smaller IMCs and a decrease in electrical resistance [41]. At the tool offset of 0.6 mm towards the Al side, the highest electrical resistivity of $0.039 \mu\Omega\text{m}$ was found. On the other hand, a 1.2 mm tool offset towards the aluminium side had a lower electrical resistivity of $0.025 \mu\Omega\text{m}$.

5.3.4 Effect of tool tilt angle

The effect of tool tilt angle on electrical resistivity of the joint is shown in Fig. 15d. It was observed that as the tool tilt angle increased and the heat input decreased, the joint's electrical resistance also decreased. Electrical resistance is observed to be decreased because there is less intense IMC production in the weld zone due to the lower heat input [12, 41].

5.4 Competence of established empirical models for σ_s and ρ

Table 5 and Table 9 shows the statistical results of the established empirical relationships. A perfect match between the expected and experimental values is shown by an R^2 value of

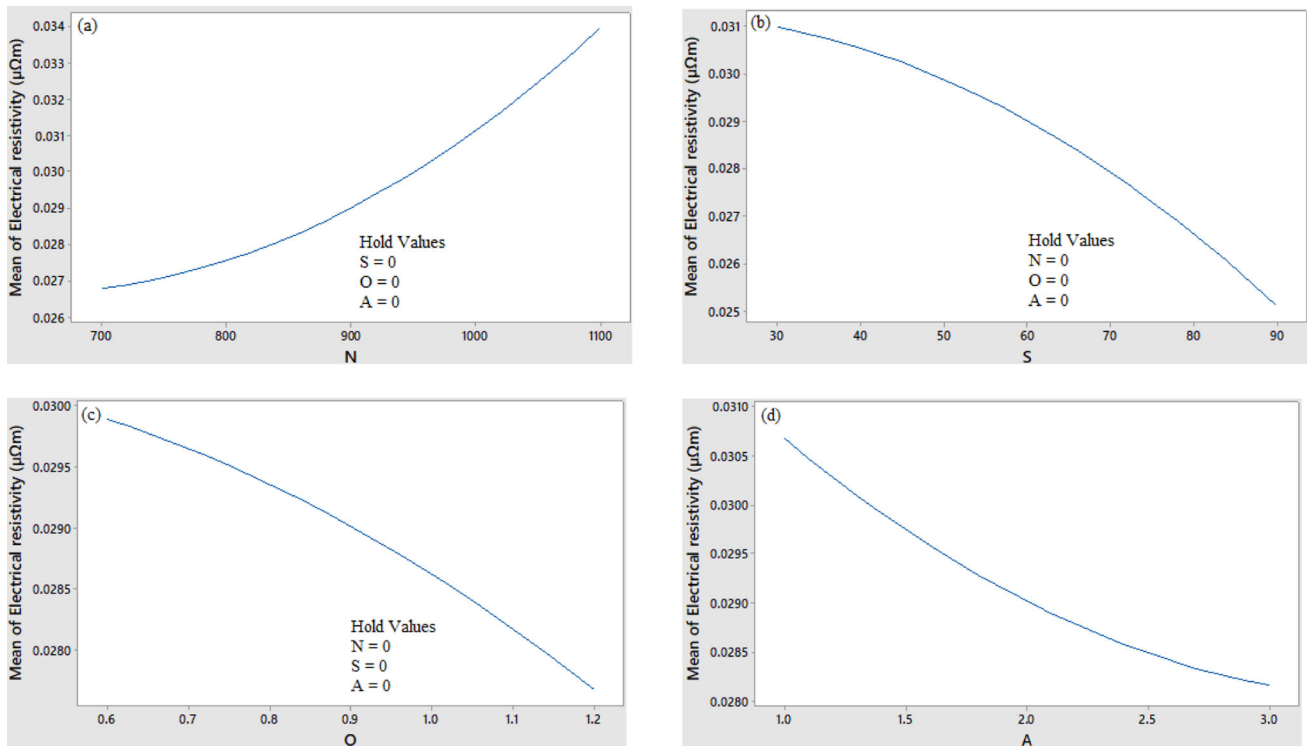


Fig. 15 Direct effects of FSW parameters on ρ include: **a** Tool rotational speed, **b** traverse speed, **c** Tool offset, **d** Tool tilt angle

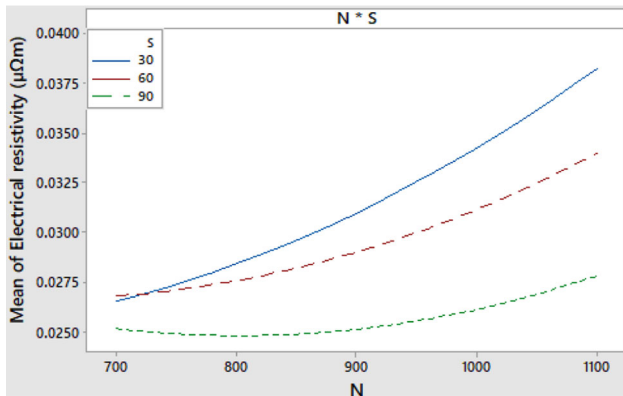


Fig. 16 Effects of N and S interacting on ρ

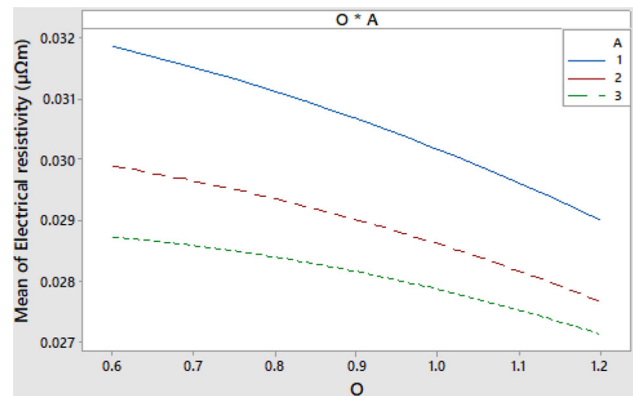


Fig. 17 Effects of N and S interacting on ρ

1. Higher R^2 values in statistical results close to 1 and lower standard error values indicate that the empirical relationship is reasonably competent and can be used to predict results accurately. More useful variables in the developed model are indicated by a higher R^2 adjusted value. The statistical findings from Table 5 revealed that σ_s had a higher R^2 value of 0.975 and an adjusted R^2 value of 0.946. Additionally, Table 9 shows that for, the higher R^2 value was 0.977 and the corrected R^2 value was 0.951. Table 6 and Table 10 shows the outcomes of the validation tests for the variables σ_s and ρ . The confirmation test results with minimal error for σ_s and ρ are presented in Table 7 and Table 11 respectively.

5.5 Optimization of FSW parameters

For maximum tensile strength, the welding parameters were optimised. The optimization was done using the MINITAB V 17 software. The optimization process uses the regression equation obtained from mathematical modelling as an objective function. For the predicted tensile strength of 179.95 MPa, the optimal tool rotational speed, traverse speed, tool offset, and tool tilt angle values are 930 rpm, 47 mm/min, 1.2 mm, and 2°, respectively. Whereas the values for the optimum input FSW parameters for the predicted electrical resistivity of the weld joint are 700 rpm for tool rotation,

Table 6 Validation test results for tensile strength

Run no.	Input parameter				σ_s (MPa)		Error σ_s %
	N	S	O	A	Experimental	Predicted	
1	1	1	0	0	163.54	164.1315	0.3604
2	- 1	- 1	0	0	155.61	155.9369	0.2096
3	0	0	- 1	1	172.61	173.6746	0.6130
4	1	- 1	0	0	163.92	164.5702	0.3951
5	- 1	1	0	0	154.04	154.3081	0.1737

Error = [(Experimental value of response - Predicted value of response)/Predicted value of response] \times 100% [39]

Table 7 Confirmation test for experimental analysis of tensile strength

Run no.	Input parameter				σ_s (MPa)		Error σ_s %
	N	S	O	A	Experimental	Predicted	
1	930	47	1.10	2	179.95	180.1060	0.087%

Table 8 Tensile strength results from an ANOVA

Source	DF	Adj SS	Adj MS	F-Value	P Value	Significance of parameter
Model	14	1953.15	139.51	33.38	0.000	-
Linear	4	287.82	71.96	17.22	0.000	-
N	1	255.49	255.49	61.14	0.000	Yes
S	1	3.02	3.02	0.72	0.412	No
O	1	28.72	28.72	6.87	0.022	Yes
A	1	0.13	0.13	0.03	0.865	No

70 mm/min for traverse, 1.2 mm for tool offset, and 3° for tool tilt angle. ANOVA Table 8, 9, 10, 11 and Table 12 show the significance of the process parameters on tensile strength and electrical resistivity. It was found that the tool rotational speed and tool offset were important parameters for tensile strength. While for electrical resistivity, each parameter was significant.

5.6 Microhardness test

From the retreating to advancing side, the microhardness test was carried out three times, at 0.5 mm (top), 2 mm (middle), and 3.5 mm (bottom) in the weld. In all three regions, there was a variation in microhardness. Due to the presence of intermetallic compounds, the weld nugget zone's bottom exhibited a peak in microhardness [43]. IMCs thicken as a result of the increased heat input in the bottom of SZ, increasing the microhardness. [43]. At the Cu side's thermo-mechanically affected zone adjacent to the weld nugget zone, a sudden increase in microhardness was observed. Due to higher heat input, the complicated structure was evident near to the shoulder area. The weld nugget zone had a wave-like distribution of microhardness. The two materials' dissimilar characteristics led to narrower TMAZ and HAZ on the Cu

Table 9 Statistical results for electrical resistivity

Response	R ²	Adjusted R ²	Standard error %
Electrical resistivity	0.977%	0.951%	0.0007792

side and broad TMAZ and HAZ on the aluminium side. The sudden peak in microhardness was caused by IMC clustering and dispersoids forming in the TMAZ of the Cu side [44].

5.6.1 Microhardness at the top

Figure 18a displays the microhardness distribution at the top. The distribution of microhardness was observed in the SZ was complex. It was as a function of IMC formation in the SZ [43]. Thus, hard IMCs were seen in the soft Al material, increasing the microhardness. Due to the IMCs getting mixed with the base materials, which increased the microhardness, variations in the microhardness were also observed in the TMAZ [43, 44]. The microhardness was between 60 and 100 HV on the Al side of the HAZ. Both sides' TMAZs

Table 10 Validation test results for electrical resistivity

Run no.	Input parameter				ρ ($\mu\Omega\text{m}$)		Error %
	N	S	O	A	Experimental	Predicted	
1	0	1	1	1	0.027	0.0259	4.25
2	0	-1	0	-1	0.032	0.0323	0.93
3	0	0	-1	1	0.030	0.0297	1.01
4	0	1	0	-1	0.030	0.0297	1.01
5	1	0	1	0	0.033	0.0340	2.94

$$\text{Error} = [(\text{Experimental value of response} - \text{Predicted value of response}) / \text{Predicted value of response}] \times 100\% \quad [39]$$

Table 11 Confirmation test for experimental analysis of electrical resistivity

Run no.	Input parameter				ρ ($\mu\Omega\text{m}$)		Error ρ ($\mu\Omega\text{m}$) %
	N	S	O	A	Experimental	Predicted	
1	700	70	1.20	2	0.025	0.0244	2.46%

Table 12 Results from ANOVA for electrical resistivity

Source	DF	Adj SS	Adj MS	F-Value	P Value	Significance of parameter
Model	14	0.000313	0.000022	36.83	0.000	–
Linear	4	0.000131	0.000033	54.06	0.000	–
N	1	0.000088	0.000088	145.02	0.000	Yes
S	1	0.000014	0.000014	22.52	0.000	Yes
O	1	0.000008	0.000008	12.48	0.004	Yes
A	1	0.000012	0.000012	19.51	0.001	Yes

displayed the sudden microhardness peak. At the Cu side, a microhardness of between 100 and 110 HV was observed.

5.6.2 Microhardness in the middle

The middle microhardness distribution is shown in Fig. 18b. The microhardness at the Al side was slightly increased up to 80 HV in the HAZ of Al side. The IMCs were mixed with the base materials to increase the microhardness, which caused fluctuations in the microhardness in the TMAZ on both sides as well as in the SZ. The formation of IMCs caused variations in the SZ to be apparent, similar to those in the top surface. The microhardness is increased by those tough and brittle IMCs. The middle microhardness distribution showed an increase in microhardness up to 100 HV on the Cu side.

5.6.3 Microhardness at the bottom

Figure 18c shows the microhardness distribution in the weld joint's bottom region. It was observed that the microhardness on the Al side of the HAZ decreased slightly from 70 to 60 HV. In the bottom of the SZ of the weld zone, drastic changes in the microhardness were observed, similar to those in the

top and centre of the SZ. This was a consequence of IMC formation in the SZ. The sudden peak in the microhardness was also seen in the TMAZ on the Al side. The level of hardness in the SZ increased when the brittle and hard IMCs were mixed with the soft aluminium material [43, 44]. The microhardness was reduced by up to 70 HV in the HAZ of the Cu side.

6 Conclusions

1. The tensile strength of the weld joints produced at the optimum process parameters of tool rotational speed of 930 rpm, traverse speed of 47 mm/min, tool offset of 1.10 mm, and tool tilt angle of 2° was 179.95 MPa.
2. The tool rotational speed, and tool offset were significant parameters whereas traverse speed and tool tilt angle were non-significant parameters for tensile strength of the weld joint.
3. The electrical resistivity of the weld joints prepared at the optimum process parameters of tool rotational speed of 700 rpm, traverse speed of 70 mm/min, tool offset of 1.2 mm, and tool tilt angle of 2° was 0.025 $\mu\Omega\text{m}$.

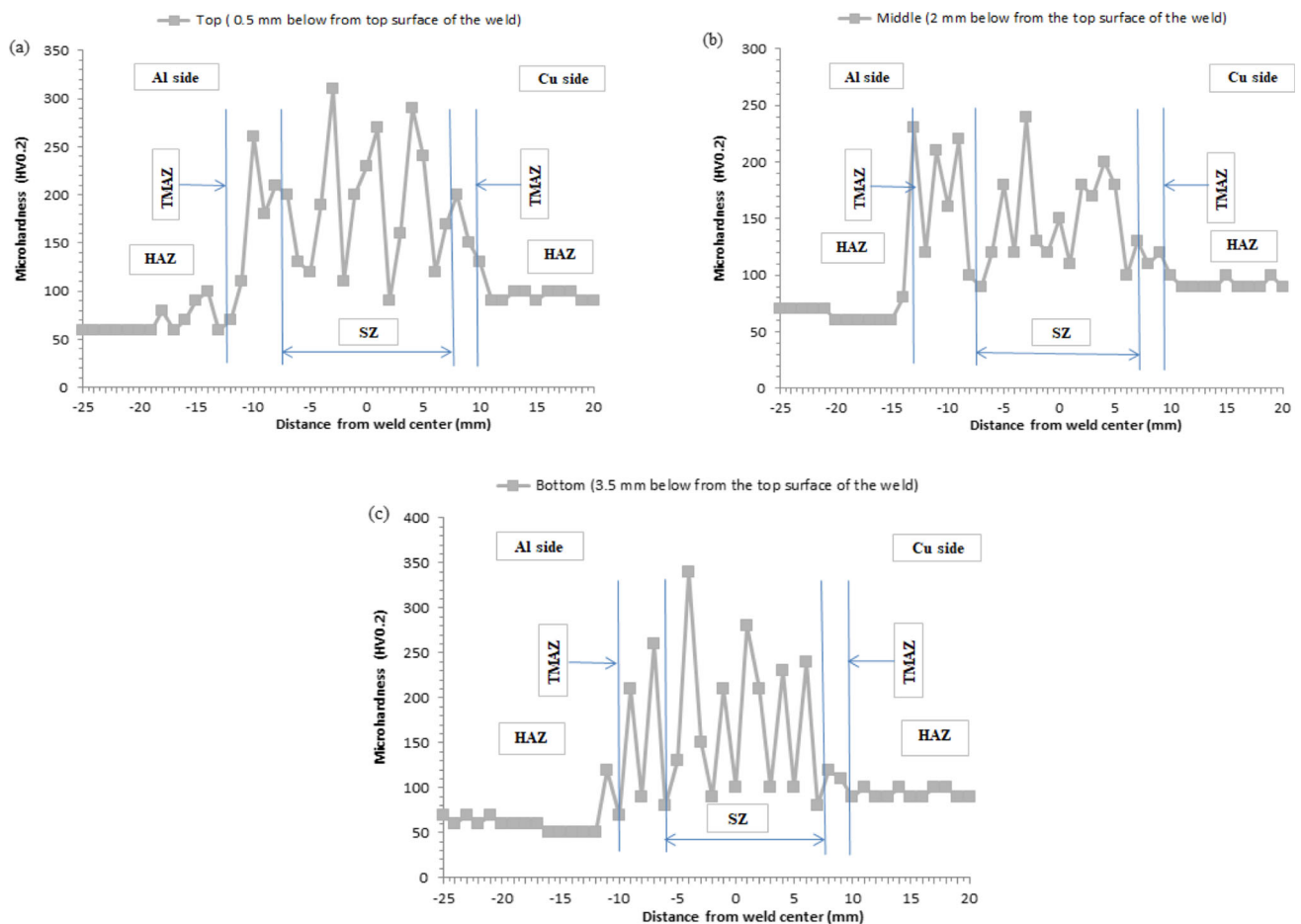


Fig.18 Microhardness distribution at optimized FSW parameters: tool rotational speed (N) 930 rpm, traverse speed (S) 47 mm/min, tool offset (O) 1.10 mm, and tool tilt angle (A) 2°

- All the parameters were significant for electrical resistivity.
- The bottom region has a peak microhardness distribution than the top and middle regions.

References

- Sare, C., Recep, C.: Effect of friction stir welding parameters on the mechanical and microstructure properties of the Al–Cu butt joint. *Metals* **6**, 1–15 (2016)
- Esmaili, A., Besharathi, M.K., Zareie Rajani, H.R.: Experimental investigation of material flow and welding defects in friction stir welding of aluminum to brass. *Mater. Manuf. Processes* **27**, 1402–1408 (2012)
- Genevois, C., Girard, M., Huneau, B., Sauvage, X., Racineux, G.: Interfacial reaction during friction stir welding of Al–Cu. *Metall. Mater. Trans.* **42**, 2290–2295 (2011)
- Muthu, M.F.X., Jayabalan, V.: Tool traverse speed effects on the microstructure of friction stir welded aluminum–copper joint. *J. Mater. Process. Technol.* **217**, 105–113 (2015)
- Li, X.-W., Zhang, D.-T., Qiu, C., Zhang, W.: Microstructure and mechanical properties of dissimilar pure copper/1350 aluminum alloy butt joints by friction stir welding. *Trans. Nonferrous Metals* **22**, 1298–1306 (2012)
- Liu, H.J., Shen, J.J., Zhou, L., Kuang, L.Y.: Microstructural characterization and mechanical properties of friction stir welded joints of aluminum alloy to copper. *Sci. Technol. Weld. Join.* **16**, 92–98 (2011)
- Galvao, I., Oliveirs, J.C., Loureiro, A., Roudrigues, D.M.: Formation and distribution of the brittle structures in friction stir welding of aluminum and copper: influence of process parameters. *Sci. Technol. Weld. Join.* **16**, 681–689 (2011)
- Fotouchi, Y., Rasae, S., Askari, A., Bisadi, H.: Effect of traverse speed of the tool on microstructure and mechanical properties in dissimilar butt friction stir welding of Al5083- copper sheets. *Eng. Solid Mech.* **2**, 239–246 (2014)
- Al-Roubaiy, A.O., Nabat, S.M., Batako, A.D.: Experimental and theoretical analysis of friction stir welding of Al–Cu joints. *Int. J. Adv. Manuf. Technol.* **71**, 1631–1642 (2014)
- Mehta, K.P., Badheka, V.J.: Experimental investigation of process parameters on defects generation on copper to AA6061-T651 friction stir welding. *Int. J. Adv. Mech. Automob. Eng.* **3**, 55–58 (2016)
- Galvao, I., Loureiro, A., Verendra, D., Gesto, D., Rodrigues, D.M.: Influence of tool offsetting on the structure and morphology of dissimilar aluminum to copper friction stir welds. *Metall. Mater. Trans.* **43A**, 5096–5105 (2012)

12. Beygi, R., Kazeminezhad, M., Kokabi, A.H.: Butt joining of Al–Cu bilayer sheet through friction stir welding. *Trans. Nonferrous Metals* **22**, 2925–2929 (2012)
13. Xue, P., Xiao, B.L., Wang, D., Ma, Z.Y.: Achieving high property friction stir welded aluminium/copper lap joint at low heat input. *Sci. Technol. Weld. Join.* **16**, 657–661 (2011)
14. Saeid, T., Abdollah-Zadeh, A.A., Saegari, B.: Weldability and mechanical properties of dissimilar aluminum–copper lap joints made by friction stir welding. *J. Alloys Compd* **490**, 652–655 (2010)
15. Shojaeefard, M.H., Khalkhali, A., Bhattacharya, O., Tahani, M.: Application of Taguchi optimization in determining aluminum to brass friction stir welding parameters. *Mater. Des.* **52**, 587–592 (2013)
16. Bisadi, H., Tavakoli, A., Sangsaraki, M.T., Sangsaraki, K.T.: The influences of rotational and welding speeds on microstructures and mechanical properties of friction stir welded Al5083 and commercially pure copper sheets lap joints. *Mater. Des.* **43**, 80–88 (2013)
17. Qui-Zheng, Z., Wen-Biao, G., Wei, L.: Microstructure and mechanical properties of dissimilar Al–Cu joints by friction stir welding. *Trans. Nonferrous Metals* **25**, 1779–1786 (2015)
18. Won-Bae, L., Kuek-Saeng, B., Seung-Boo, J.: Effects of intermetallic compound on the electrical and mechanical properties of friction stir welded Cu/Al bimetallic joints during annealing. *J. Alloy. Compd.* **390**, 212–219 (2005)
19. Paul, K., Vimalraj, C., Martikainen, J., Suoranta, R.: Factors influencing Al–Cu weld properties by intermetallic compound formation. *Int. J. Mech. Mater. Eng.* **10**, 1–13 (2015)
20. Bergmann, J.P., Schiirer, R., Schneider, S.: Solid state welding of aluminum to copper—case studies. *Wed. World* **57**, 541–550 (2013)
21. Lee, W.B., Jung, S.B.: Void free friction stir weld zone of the dissimilar 6061 aluminum and copper joint by shifting the tool insertion location. *Mat. Res. Innov.* (2016). <https://doi.org/10.1080/14328917.2004.11784837>
22. Rai, R., De, A., Bhadeshia, H.K.D.H., DebRoy, T.: Review: friction stir welding tools. *Sci. Technol. Weld. Join.* **16**, 325–342 (2011)
23. Dharmalingam, S., Lenin, K.: Effect of friction stir welding parameters on microstructure and mechanical properties of the dissimilar AA7475-AA8011 joints. *Mater. Today* (2020). <https://doi.org/10.1016/j.matpr.2020.06.317>
24. Esmaili, A., Besharati Givi, M.K., Zareie, H.R.: A metallurgical and mechanical study on dissimilar friction stir welding of aluminum 1050 to brass (CuZn30). *Mater. Sci. Eng. A* **528**, 7093–7102 (2011)
25. Zhang, Y.N., Cao, X., Wanra, P.: Review of tools for friction stir welding and processing. *Can. Metall. Q.* **51**, 250–261 (2012)
26. Zhao, X., Dong, F.B., Su, G.Y., Guo, L.J.: Weld quality improvement with hybrid FSW technology assisted by preheating for copper T2/Aluminum 5A06 dissimilar materials. *Appl. Mech. Meter.* **121**, 1707–1711 (2012)
27. Akinlabi, E.T., Akinlabi, S.A.: Effect of heat input on the properties of dissimilar friction stir welds of aluminum and copper. *Am. J. Mater. Sci.* **2**, 147–152 (2012)
28. Beygi, R., Kazeminezhad, M., Kokabi, A.H.: Microstructural evolution and fracture behavior. *Metall. Mater. Trans.* **45A**, 361–369 (2014)
29. Bhattacharya, T.K., Das, H., Pal, T.K.: Influence of welding parameters on material flow, mechanical property and intermetallic characterization of friction stir welded AA6063 to HCP copper dissimilar butt joint without offset. *Trans. Non Ferrous Metals Soc.* **25**, 2833–2846 (2015)
30. Mehta, K.P., Badheka, V.J.: Influence of tool pin design on properties of dissimilar copper to aluminum friction stir welding. *Trans. Nonferrous Metals* **27**, 36–54 (2017)
31. Mishra, R.S., De, P.S.: Friction stir welding and processing. Springer International Publishing Switzerland, Cham (2014)
32. Wei, Y., Li, H., Xiao, P., Zou, J.: Microstructure and conductivity of the Al–Cu joint processed by friction stir welding. *Adv. Mater. Sci. Eng.* (2014). <https://doi.org/10.1155/2020/6845468>
33. Argesi, F.B., Shamsipur, A., Miasalehi, S.E.: Dissimilar joining of pure copper to aluminum alloy via stir welding. *Acta Metall. Sin.* **31**, 1183–1196 (2017)
34. Ashok, J., Shridhar, N., Arumani, L., Santosh, H.: A review on friction stir welded aluminum copper specimens. *Adv. Mater. Process. Technol.* (2020). <https://doi.org/10.1080/2374068X.2020.1855403>
35. Koilraj, M., Sundareswaran, V., Vijayan, S., Koteswara, R.S.: Friction stir welding of dissimilar aluminum alloys AA2219 to AA5083—optimization of process parameters using Taguchi technique. *Mater. Des.* **42**, 1–7 (2012)
36. Sharma, N., Khan, Z.A., Siddiquee, A.N., Wahid, M.A.: Multi-response optimization of friction stir welding parameters for dissimilar joining of Al6101 to pure copper using standard deviation based TOPSIS method. *J. Mech. Eng. Sci.* (2019). <https://doi.org/10.1177/0954406219858628>
37. Verma, S., Kumar, V.: Optimization of friction stir welding parameters of dissimilar aluminum alloys 6061 and 5083 by using response surface methodology. *J. Mech. Eng. Sci.* (2021). <https://doi.org/10.1177/09544062211005804>
38. Elnabi, M.A., Mokadem, A.E., Osman, T.: Optimization of process parameters for friction stir welding of dissimilar aluminum alloys using different Taguchi arrays. *Int. J. Adv. Manuf. Technol.* **121**, 3935–3964 (2022)
39. Shanavas, S., Dhas, J.E.: Parametric optimization of friction stir welding parameters of marine grade aluminum alloy using response surface methodology. *Trans. Nonferrous Metals Society China* **27**, 2334–2344 (2017)
40. Mehta, K.P., Badheka, V.J.: A review on dissimilar friction stir welding of copper to aluminum: process, properties, and variants. *Mater. Manu. Process* **31**, 233–254 (2015)
41. Abbasi, M., Teheri, A., Salehi, M.: Growth rate of intermetallic compounds in Al/Cu bimetal produced by cold roll welding process. *J. Alloys Compd.* **319**, 233–241 (2001)
42. Fotouchi, Y., Rasaei, S., Askari, A., Bisadi, H.: Effect of traverse speed of the tool on microstructure and mechanical properties in dissimilar butt friction stir welding of Al5083–copper sheets. *Eng. Solid Mech.* **2**, 239–246 (2014)
43. Xue, P., Xiao, B.L., Ni, D.R., Ma, Z.Y.: Enhanced mechanical properties of friction stir welded dissimilar Al–Cu joint by intermetallic compound. *Mater. Sci. Eng. A* **527**, 5723–5727 (2010)
44. Murr, L.E., Li, Y., Flores, R.D., Trillo, E.A.: Intercalation vortices and related microstructural features in the friction stir welding of dissimilar metal. *Mater. Res. Innov.* **2**, 150–163 (1998)
45. Kah, P., Rajan, R., Martikainen, J., Suoranta, R.: Investigation of weld defects in friction stir welding and fusion welding of aluminum alloys. *Int. J. Mech. Mater. Eng.* **26**, 1–10 (2015)
46. Jabbari, M., Tutum, C.: Optimum rotation speed for the friction stir welding of pure copper, pp. 1–6. Hindawi Publishing Corporation, London (2013)
47. Manickam, S., Balsubramanian, V.: Optimizing the friction stir spot welding parameters to attain maximum strength in Al.Mg dissimilar. *J. Weld. Join.* **34**(3), 23–31 (2016)
48. Ibrahim, S., Nabil, G., Abdul, M.G., Abdel, M.: Optimization of process parameters to maximize ultimate tensile strength and hardness of underwater friction stir welded aluminum alloys using fuzzy logic. *Mod. Concepts Mater. Sci.* **3**(1), 1–11 (2020)
49. Van, A., Nguyen, T.: Optimization of friction stir welding operation using optimal taguchi based ANFIS and genetic algorithm. *J. Mech. Eng.* **68**, 424–438 (2022)

50. Prabhu, S., Shetigar, A., Herbert, M., Rao, S.: Parameters investigation and optimization of friction stir welded AA6061/TiO₂ composites through TLBO. *Weld. World* **103**, 93–103 (2021)
51. Hussain R.M., Abdullah Al-Shammari M.: Optimization of friction stir welded aluminum plates by the new modified particle swarm optimization. In: IOP Conference, Materials Science and Engineering, vol. **1094**, pp. 1–10 (2020)
52. Xue P., Xiao B.L., Ma Z.Y.: Effect of interfacial microstructure evolution on mechanical properties and fracture behavior of friction stir welded Al-Cu joints. *Metall. Mater. Trans. A*, 1–13 (2015)
53. Dond, D., Gulhane, N.: Optimization of injection system parameter for CRDI small cylinder diesel engine using response surface method. *J. Ind. Eng.* **102**, 1007–1029 (2021)
54. Murr, L.E., Flores, R.D., Flores, O.V.: Friction stir welding: microstructural characterization. *Mat. Res. Innovat.* **223**, 211–223 (1998)
55. Section IV, Chapter 13, Bus conductor design and applications. pp. 1–70.

Publisher's Note Springer Nature remains neutral with regard to jurisdictional claims in published maps and institutional affiliations.

Springer Nature or its licensor (e.g. a society or other partner) holds exclusive rights to this article under a publishing agreement with the author(s) or other rightsholder(s); author self-archiving of the accepted manuscript version of this article is solely governed by the terms of such publishing agreement and applicable law.